encit 2020

ABCM
Associação Brasileira de Engenharia e Ciências Mecânicas

18th Brazilian Congress of Thermal Sciences and Engineering
November 16–20, 2020 (Online)

ENC-2020-0520
COMPUTATIONAL FLUID DYNAMICS FOR WIND FARM PERFORMANCE ASSESSMENT IN COMPLEX TERRAIN

William Corrêa Radünz
Laboratory of Energy Conversion Engineering and Energy Technology, Federal University of Santa Catarina
w.radunz@posgrad.ufsc.br

Yoshiaki Sakagami
Department of Health and Service, Federal Institute of Santa Catarina
yoshi@ifsc.edu.br

Reinaldo Haas
Department of Physics, Federal University of Santa Catarina
reinaldohaas@gmail.com

Júlio César Passos
Department of Mechanical Engineering, Federal University of Santa Catarina
julio.passos@lepten.ufsc.br

Adriane Prisco Petry
Department of Mechanical Engineering, Federal University of Rio Grande do Sul
adrianep@mecanica.ufrgs.br

Mayara Miqueletti
Eduardo Dias
CGN Brasil Energia e Participações S.A
mayara.lima@cgnbe.com.br; eduardo.dias@cgnbe.com.br

Abstract. *Atmospheric stability influences local flow dynamics in complex terrains and may therefore impact turbine production across the wind farm area. Field measurements and wind farm production data gathered at the sited revealed a systematic overperformance of the back row during stable conditions. This pattern is inverted during unstable conditions and the same back rows underperform in comparison with the front rows. Here we employ a novel framework for the simulation of unsteady and stably-stratified wind flows in complex terrain areas that is based on the coupling of a microscale computational fluid dynamics (CFD) model and a mesoscale numerical weather prediction (NWP) model is employed to enhance our understanding of the flow patterns in the wind farm area. Simulations are not intended to reproduce the wind conditions of the site in detail, but rather to perform a proof of concept: that the inversion in performance observed is explainable by the wind patterns and their interplay with atmospheric stability. Indeed, wind flow patterns are largely different between unstable and stable conditions and the numerical simulations are successful in emulating how the wind farm operates.*

Keywords: *atmospheric stability, complex terrain, wind farm performance, CFD, NWP*

1. INTRODUCTION

The past few years have been marked by large-scale multi-disciplinary wind mapping project in complex terrain sites to enhance our comprehension of the mesoscale and microscale physical processes in the atmospheric boundary-layer (Mann *et al.*, 2017; Fernando *et al.*, 2019; Barthelmie and Pryor, 2019). Those dedicated campaigns typically deploy a dense array of met masts and/or scanning lidars to observe wind patterns as they change according to atmospheric conditions (Mann *et al.*, 2017), therein providing observational evidence to foster the development of a new generation of model chains (Sanz Rodrigo *et al.*, 2017b). However, few kinds of research involved how such wind conditions influence the performance of operational wind farms in complex terrain. Evidence of the interplay between factors such as atmospheric

stability and topography on farm performance is fundamental in that the end product of novel wind resource assessment techniques is an accurate representation of turbine power or energy yield. In that endeavor, SCADA and mast data provide accurate information on this behavior. Their joint employment with computational fluid dynamics (CFD) may help to shed light on this matter, as CFD provides a representation of the whole three-dimensional wind speed field. The usage of CFD for wind resource mapping in complex terrain areas is a field of intensive research (Radünz *et al.*, 2020a), and the ideally superior capabilities of the novel model chains in simulating the interplay between wind patterns, topography and atmospheric stability may play a main role in improving wind farm projects soon.

Measurements at a wind farm built over a small plateau area in Northeast Brazil revealed a strong relationship between atmospheric stability and farm power performance across the diurnal cycle. One of the hypotheses raise was that the interplay between topography and atmospheric stability produced significantly different flow patterns, which in turn impacted the operation of the wind farm. In this context, our goal is to test this hypothesis via a proof of concept: employing a novel wind flow simulation framework to assess whether the aforementioned performance patterns are explainable by the proposed hypothesis.

Section 2 describes the wind farm site and the numerical model framework. Section 3 reports on the measured power performance patterns and the outcomes from the numerical simulations. Section 4 summarizes the main outcomes of this investigation.

2. METHODOLOGY

2.1 Site description

The Campo Formoso I (CF1) wind farm is composed of 15 turbines and belongs to a larger wind farm complex that is known as Morrinhos. The latter is located roughly 360 km from the coast of the Atlantic Ocean, in Bahia, Northeast Brazil. Fig. 1 shows the layout of the wind farm overlayed to the digital elevation map. Turbines are sited on top of a plateau area to harness additional power from the topographic acceleration of the winds: the front row contains 8 turbines and the back row contains 7 turbines. These bear the same specifications, such as nameplate power of 2 MW and a hub height of 78 m. There are additional turbines that belong to other wind farms immediately north of CF1, but those are out of the scope of this investigation.

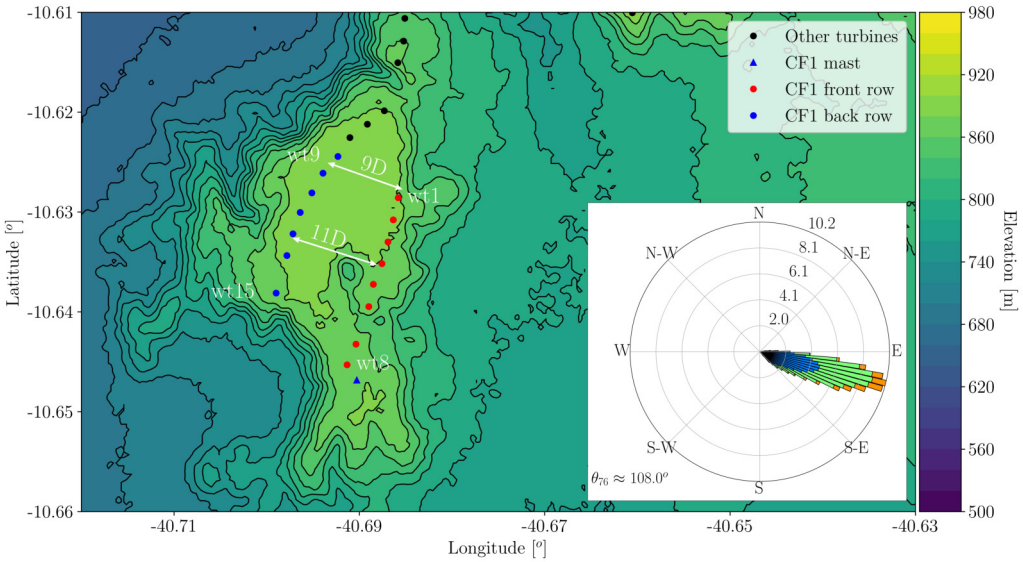

Figure 1. Layout of the Campo Formoso I (CF1) wind farm that is located in the Morrinhos wind farm complex in Brazil. The wind direction rose was measured with a wind vane installed at 76 m at the met mast.

Winds at the site are predominantly east southeastern (ESE) with a mean wind direction of 108. This inflow direction is roughly orthogonal to the turbine arrays and the plateau slopes, and the interplay between winds and topography can lead to intricate flow patterns such as separation and recirculation, especially near the abrupt elevation loss of about 200 m immediately downstream of the back rows. These flow patterns are usually sensitive to atmospheric stability conditions. The latter was considered in this investigation via observations from a sonic anemometer that was installed in the met mast at 10 m above ground. It measures the three components of wind speed, and temperature, at a sampling rate of 20 Hz. A thorough description of how the spatial variability of wind resources is affected by atmospheric stability conditions may be found in (Radünz *et al.*, 2020b).

2.2 Atmospheric stability classification

Atmospheric stability here is addressed and described based on the Monin-Obukhov similarity theory (MOST) framework (Monin and Obukhov, 1954; Foken, 2006). A central parameter within this theoretical framework is the Obukhov length (L), which is the length scale associated with the relative contribution of buoyancy, in contrast to mechanical shear, in the production of turbulence kinetic energy (TKE). The Obukhov length is given by

$$L = -\frac{u_\star^3}{\kappa \left(\frac{g}{\theta_v}\right)\left(\frac{H_s}{\rho c_p}\right)}, \tag{1}$$

where $u_\star$ is the friction velocity, H_s is the sensible heat flux, κ is the von Kármán constant (≈ 0.40), ρ stands for air density, c_p is the specific heat of air, g is the gravity acceleration (≈ 9.81 m/s) and θ_v is the surface potential temperature.

The Obukhov length is indirectly obtained via the computation of the friction velocity and the sensible heat flux, which are in turn calculated via the well-consolidated eddy covariance technique (Lee *et al.*, 2004). The computation of the turbulent fluxes based on the high-frequency measurements from the sonic anemometer was performed with the open-source software EddyPro v. 6.2.2 (LI-COR Biosciences, 2019). The $u_\star$ and H_s were thus obtained via the following expressions

$$u_\star = \left[(\overline{u'w'})^2 + (\overline{v'w'})^2\right]^{1/4}, \tag{2}$$

$$H_s = \rho c_p \overline{\theta_v' w'}, \tag{3}$$

where $\overline{u'w'}$ and $\overline{v'w'}$ represent the turbulent *momentum* fluxes and $\overline{\theta_v' w'}$ is the kinematic heat flux at the surface. The $u_\star$ and H_s variables are calculated as hourly averages, which is a timescale sufficiently long to include the contributions of the motions of the largest eddies in the atmospheric boundary-layer (Lee *et al.*, 2004). The dataset is subsequently linearly resampled as 10-minute averages to synchronize with the turbine production data. Table 1 enables a qualitative description of the stability conditions based on the L parameter (Wharton and Lundquist, 2012).

Table 1. Atmospheric stability classes segregated by L ranges based on (Wharton and Lundquist, 2012).

Class	L ranges [m]
Very unstable	$-50 \leq L < 0$
Unstable	$-600 \leq L < -50$
Neutral	$L < -600$ or $L \geq 600$
Stable	$100 \leq L < 600$
Very stable	$0 \leq L < 100$

2.3 CFD modeling framework

The mesoscale-to-microscale modeling framework has been developed at the National Renewable Energy Centre (CENER). The microscale model is built within the open-source CFD toolbox OpenFOAM, which implements the finite volume method (FVM) to solve conservation equations (Weller *et al.*, 2002).

More detailed information regarding the proof-of-concept of the coupling approach based on mesoscale tendencies is found in (Sanz Rodrigo *et al.*, 2017a), and (Chávez Arroyo *et al.*, 2018) provides an investigation focused on the evaluation and processing of mesoscale tendencies. In (Sanz Rodrigo *et al.*, 2017c), a more detailed validation of the modeling framework is carried out using a single-column modeling approach – that is, the CFD domain is simplified as a vertical column with several cells in the z direction, whereas in the x–y plane a single (or a couple) of cells are used. This is to test the method whilst sparing computational resources.

Those studies assume a flat terrain area, which is certainly not the case for our investigation. Thus, this paper also provides interesting testing of the framework at a complex terrain site.

2.3.1 Microscale model

To enable the solution of the diurnal cycle, the temporal derivative is retained within the equations and the problem is modeled via an unsteady RANS (URANS) paradigm. The continuity, *momentum* and temperature URANS equations for incompressible flows are given by the following expressions shown in index notation (i, j = 1, 2, 3):

$$\frac{\partial \rho U_i}{\partial x_i} = 0, \tag{4}$$

$$\frac{\partial \rho U_i}{\partial t} = \frac{\partial}{\partial x_j}\left[-\rho U_i U_j + (\mu + \mu_t)\left(\frac{\partial U_i}{\partial x_j} + \frac{\partial U_j}{\partial x_i}\right)\right] - \frac{\partial p}{\partial x_i} + g_i(\rho - \rho_0) + \epsilon_{ijk} f_c \rho U_k + \rho F_{U,i}, \tag{5}$$

$$\frac{\partial \rho \theta}{\partial t} + \frac{\partial \rho U_i \theta}{\partial x_i} - \frac{\partial}{\partial x_i}\left[\left(\mu + \frac{\mu_t}{\sigma_\theta}\right)\frac{\partial \theta}{\partial x_i}\right] = \rho F_\theta, \tag{6}$$

where U_i is the mean wind speed, θ_i the mean potential temperature, f_c is the Coriolis parameter (f_c = 2 $\Omega sin\lambda$), ϵ_{ijk}^T = (-1,1,0), Ω is the rotation of the Earth (7.272 x 10^{-5} rad/s), λ denotes latitude, μ is the dynamic viscosity. The terms $F_{U,i}$ and F_θ represent *momentum* and temperature source terms.

The potential temperature equation is coupled with the *momentum* equations through the buoyancy force term $g_i(\rho - \rho_0)$ (where ρ_0 = 1.225 kg/m^3). The Boussinesq approximation is employed, and as such, variations in ρ neglect the influence of pressure variations and the flow may be treated as incompressible. Therein, density does not depend on pressure and obeys the following relationship based on the ideal gas law:

$$\rho = \frac{M p_0}{RT} \tag{7}$$

here, M is the molar mass of air (29 g mol^{-1}), p_0 is the standard atmospheric pressure at mean sea level (10^5 Pa) and R is the universal gas constant (8.313 J K mol$^-1$). In Eq. (8), temperature is replaced by the potential temperature as follows,

$$\theta = T\left(\frac{p_0}{p}\right)^{R/c_p}, \tag{8}$$

here, the specific heat capacity for dry air is taken as $c_p \approx 1$ kJ $kg^{-1}K^{-1}$ and the modified pressure term p' is the total pressure assuming hydrostatic equilibrium ($p' = p + \rho_0 gz$).

2.3.2 Turbulence model

The eddy viscosity term present in Eq. (5) and (6) is computed via a modified version of the standard *k*-ϵ model (Launder and Spalding, 1974) that includes additional source terms at the right-hand side of the turbulence kinetic energy (TKE, k) and its dissipation rate (ϵ) to account for buoyancy that was originally proposed by (Sogachev *et al.*, 2012)

$$\frac{\partial k}{\partial t} + U_i\frac{\partial k}{\partial x_i} - \frac{\partial}{\partial x_i}\left[\left(\nu + \frac{\nu_t}{\sigma_k}\right)\frac{\partial k}{\partial x_i}\right] = P + B - \epsilon + \epsilon_a, \tag{9}$$

$$\frac{\partial \epsilon}{\partial t} + U_i\frac{\partial \epsilon}{\partial x_i} - \frac{\partial}{\partial x_i}\left[\left(\nu + \frac{\nu_t}{\sigma_\epsilon}\right)\frac{\partial \epsilon}{\partial x_i}\right] = \frac{\epsilon}{k}C_{\epsilon 1}^* P + C_{\epsilon 3}^* B - C_{\epsilon 2}^*\epsilon\Big) + C_{\epsilon 2}^*\frac{\epsilon_a^2}{k_a}, \tag{10}$$

where the shear turbulent production term (P) is positive and always increases k, whereas the buoyant term (B) leads to either production or dissipation of k depending on its sign,

$$P = \nu_t\left(\frac{\partial U_i}{\partial x_j} + \frac{\partial U_j}{\partial x_i}\right)\frac{\partial U_i}{\partial x_j}, \tag{11}$$

$$B = -\frac{\nu_t}{\sigma_\theta}\frac{g_i}{\theta}\frac{\partial \theta}{\partial x_i}. \tag{12}$$

Thus, under unstable stability conditions the vertical gradient is negative ($\frac{\partial \theta}{\partial x_i} < 0$) and produces positive B (upward buoyancy), whereas under stable stability conditions the vertical gradient is positive ($\frac{\partial \theta}{\partial x_i} > 0$) and produces negative B (downward buoyancy). Ultimately, the eddy viscosity is computed as

$$\nu_t = C_\mu\frac{k^2}{\epsilon} = C_\mu^{1/4}k^{1/2}l, \tag{13}$$

where the characteristic length scale associated with turbulent eddies is obtained as follows

$$l = C_\mu^{3/4}\frac{k^{3/2}}{\epsilon}. \tag{14}$$

It is well known that the standard *k*-ϵ model is overly diffusive, which produces an exaggerated length scale (l), especially farther from the terrain surface. Therefore, as length scale limiter was proposed to account for changes in the

maximum size of turbulent eddies that are naturally caused either by the ABL height or thermal stratification, which is expressed as

$$C^*_{\epsilon 1} = C_{\epsilon 1} + (C_{\epsilon 2} - C_{\epsilon 1})\frac{l}{l_{max}}. \tag{15}$$

Therefore, when the mixing length (l) reaches the upper limit (l_{max}), it leads to $C^*_{\epsilon 1} = C^{\epsilon 2}$. This means production and dissipation terms in Eq. (10) are in equilibrium. Conversely, when l is sufficiently smaller than l_{max}, $C^*_{\epsilon 1} \approx C^{\epsilon 1}$. This is usually the case near ground where dissipation is expressive, and as such the model retains the traditional log-law shape there. The maximum length scale (l_{max}) is computed as (Sogachev *et al.*, 2012)

$$l_{max} = \alpha \frac{\int_0^\infty z\sqrt{k}dz}{\int_0^\infty \sqrt{k}dz} \tag{16}$$

where $\alpha = 0.075$, thus complying with the vertically constant l associated with neutral stability conditions (l_{max} = 0.00026 Gf_c^{-1}, where $G = \sqrt{U_g^2 + V_g^2}$ is the geostrophic wind). The following expression ensures overall model consistency near ground

$$\sigma_\epsilon = \frac{k^2}{C_\mu^{1/2}(C_{\epsilon 2} - C_{\epsilon 1})}. \tag{17}$$

Additional modifications proposed by (Sogachev *et al.*, 2012) enabled the model to become self-consistent while establishing a relationship with other existing models constants

$$C_{\epsilon 3} = (C_{\epsilon 2} - C_{\epsilon 1})\alpha_B + 1, \tag{18}$$

Ultimately, the friction velocity and sensible heat flux are computed as

$$u_\star^2 = -\mu_t \left(\frac{\partial U_i}{\partial x_j} + \frac{\partial U_j}{\partial x_i} \right), \tag{19}$$

$$H_s = \frac{\mu_t}{\sigma_\theta}\frac{\partial \theta}{\partial z}. \tag{20}$$

2.4 Power performance

Power performance (ϵ_P) is here defined as the relative difference in mean power (P) between the two rows of turbines. It is expressed in percentage as follows:

$$\epsilon_P = \frac{(P_{front} - P_{back})}{P_{back}} 100. \tag{21}$$

Here, P_{back} denotes the mean power of the cluster of turbines located downstream of the first row in the prevailing wind direction, whereas P_{front} refers to the mean power of the front row. As for the ϵ_P value obtained from the CFD simulations, it is computed based on the cube of the horizontal wind speeds (U^3) as an analogy with the wind power density concept (Radünz *et al.*, 2020a).

3. RESULTS AND DISCUSSION

The goal here is to emulate the characteristics of the morning and the evening transition periods rather than reproduce those in detail by tuning initial conditions and parameters to match observations.

The morning transition is the development of a new layer near the ground because of the onset of thermal convection because of the surface heating by the sun. So, the formerly neutral or stable layer becomes either unstable or very unstable. Conversely, near sunset, the surface loses heat via radiational cooling very rapidly and becomes colder than the surrounding air. This initiates a process by which heat is removed from the overlying air and transferred toward the ground surface, and thus air near the surface is colder than aloft. In these situations the formerly unstable or very unstable layer transitions toward a stable or very stable layer.

These situations are produced here departing from a fully neutral initial condition for which the potential temperature everywhere, including the initial surface potential temperature, is set to 300 K. Next the surface temperature will change over two hours (which are the total simulation time) based on a specified temporal gradient ($\Delta T/\Delta t$).

Thus, this section first reports on the observational evidence of the power performance patterns at the wind farm; the focus is on the interplay between the performance metric ϵ_P, atmospheric stability conditions and the diurnal cycle. Then, the latter is compared with the CFD simulations.

3.1 Field observations

The field observations and turbine production data employed here are associated with the period between November 2018 to July 2019. A thorough description of wind resources and atmospheric stability conditions at the site may be found in (Radünz *et al.*, 2020b). Fig. 2a shows the typical frequency of occurrence of certain atmospheric stability classes as the diurnal cycle evolves. The daytime period from sunrise (06:00) to sunset (18:00) is mostly unstable and very unstable because of the ground surface heating by the sun, whereas the nighttime period (19:00 to 05:00) consists of a combination of neutral, stable and very stable conditions. The aforementioned morning (06:00 to 08:00) and evening (17:00 to 19:00) transition periods are clearly illustrated as rapid changes in atmospheric stability conditions over periods of roughly two hours.

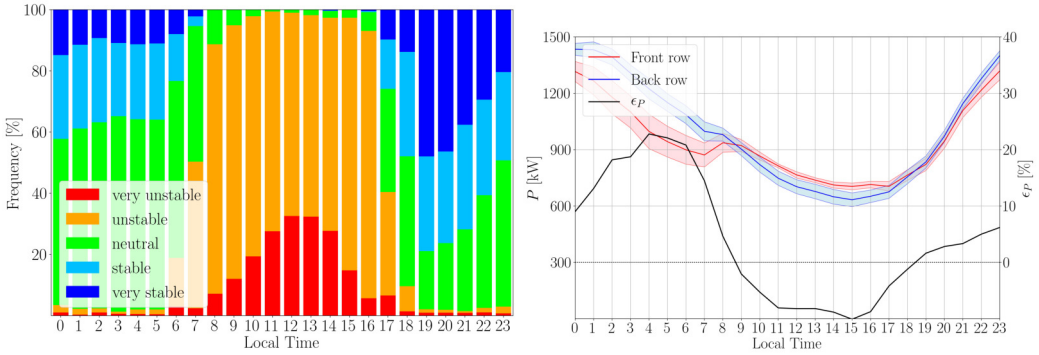

(a) (b)

Figure 2. Mean power segregated by turbine clusters at CF1 reveals that a front-back row configuration produces a performance inversion associated with different degrees of atmospheric stability based on the hour of the day.

The diurnal cycle of atmospheric stability conditions appears to have paramount influence in the way the wind farm typically performs (Fig. 2b). Here, the mean power of the front and back rows is separately represented as red and blue lines, respectively. The shaded envelopes represent one standard deviation of the intra-row variability. The mean values were calculated based on 10-minute production data obtained from a Supervisory Control and Data Acquisition (SCADA) system at the wind farm. Nighttime production is overall larger than daytime production owing to the typically strong nocturnal winds at the site. The performance metric appears as a black line.

The mean performance patterns change throughout the day, with an underperformance (of the back row relative to the front row) between 09:00 and 18:00, and with an overperformance between 19:00 and 08:00. During the day, the underperformance can reach close to -10%, whereas during the night the overperformance can be, on average, greater than 20%. Because the diurnal cycle contains a combination of different stability classes (such as neutral, stable and very stable conditions during the nighttime), their influence on performance is diluted. That is, stable and very stable conditions alone should cause a larger overperformance than when neutral conditions are also considered.

At the onset of unstable conditions between 06:00 and 08:00, ϵ_P rapidly decreases toward negative values. At the onset of stable conditions between 17:00 and 19:00, ϵ_P increases toward larger and positive values. Thus, our goal with the CFD simulations is to represent those two-hour periods departing from identical initial conditions at which the atmospheric boundary layer is neutrally stratified, and in which the ground surface either starts to heat-up or cool-down, causing the onset of unstable or stable conditions, respectively.

3.2 Numerical simulations

Because the modeling paradigm involves the forcing of flow using mesoscale tendencies (which resembles a pressure gradient in a wind tunnel) and not inflow-outflow-type boundary conditions, cyclic boundary conditions are specified for all calculated fields at the four domain sides shown in Fig. 3a. The flow near the ground was modeled by wall-functions and surface roughness (z_0 = 0.23 m) was adopted based on (Radünz *et al.*, 2020b). We used adjustable timestep to limit the maximum Courant number to 0.75, single wind direction (westerly wind, or 90 inflow direction) and the Coriolis effect is neglected – $f_c = 0$ in Eq. 5 because we are assuming the location is sufficiently close to the Equator ($\lambda \approx 0$). As a matter of fact, the location is 10 south of the Equator.

The computational domain consists of a 10.4 km x 11 km x 2 km box (Fig. 3a), in which the digital elevation model of the terrain is found at the bottom (Fig. 3b). The latter has been smoothed and flattened to flat horizons farther from the region of interest because the usage of cyclic conditions requires identical boundary patches on the sides. The grid was generated using OpenFOAM's native tool for unstructured meshes *snappyHexMesh*. It is mostly constituted of hexagons with three different refinement levels. At the coarsest level near the top of the domain, the hexagons are composed of 50 m edges. These are halved across different refinement levels, ultimately reaching 12.5 m close to ground level. There,

an additional layer has three prisms of 5-m-height to improve the computation of gradients and wall-functions near the ground. The overall mesh cell count is 785,098.

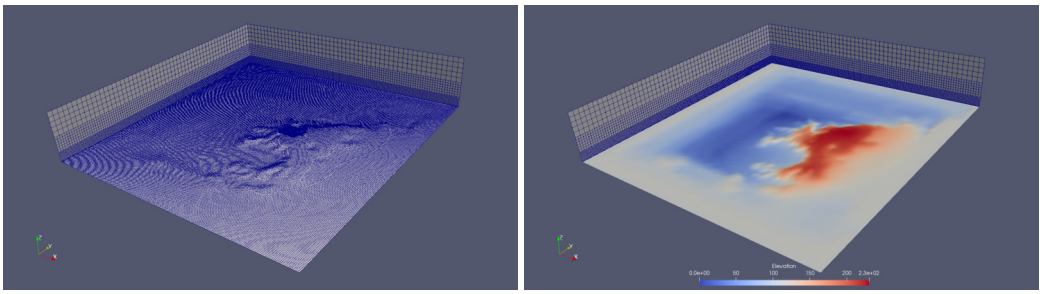

(a) (b)

Figure 3. Computational grid of 785,098 cells of the wind farm area (a) and a digital elevation map of the terrain (b).

The synthetic wind speed and temperature fields are illustrated in Figs. 4a-b, respectively. Wind speeds are negative because the westerlies (90 direction) flows opposite to the x-axis. The fields related to turbulence, such as k and ϵ, have been initialized based on the GABLS experiment (Sanz Rodrigo *et al.*, 2017a), which is available as an option within the CFDWind3 framework. Anyhow, the focus is on how the flow evolves and these idealized initializations should be sufficient for this purpose.

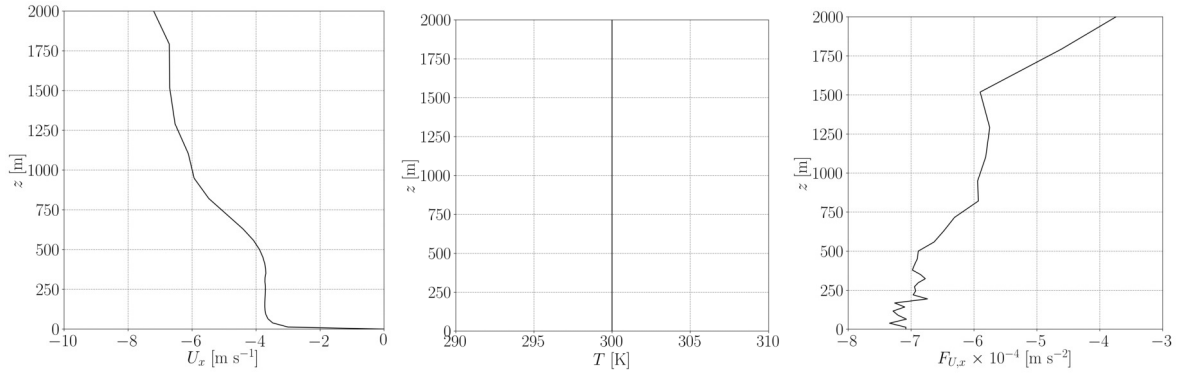

(a) (b) (c)

Figure 4. Initial wind speed (a), potential temperature (b) and x-component of the mesoscale momentum forcing (c) values prescribed within the computational domain.

The instantaneous wind patters occurring after 2 hours of simulation are represented by the streamlines (Fig. 5a-b) and wind speed maps (Fig. 5c-d). For the unstable case (Fig. 5a), streamlines fluctuate vertically across the simulation domain as a consequence of the upward buoyancy. The latter significantly enhanced the unsteadiness, turbulent mixing and gustiness of the wind. An interesting feature appears during stable conditions (Fig. 5b), which is the dividing streamline concept Silver *et al.* (2018). That is, in stable conditions the denser air near the ground may flow around obstacles instead of flowing over them. This feature creates a river-like behavior in which the streamlines gently flow in three separate regions. Two of those flow around the plateau area, whereas a third one flows over the topography. Wind patterns at a constant height of 80 m above ground illustrate the enhanced gustiness of unstable flows (Fig. 5c) and the more gentle character of stable flows (Fig. 5d).

The x component of the wind speed (U_x), the potential temperature (T) and the TKE (k) fields have been sliced along the x-direction at the center of the domain and averaged over two hours. These are shown both for unstable (Figs. 6a,c,e) and stable (Figs. 6b,d,f) conditions.

Wind speed magnitudes are rather comparable between unstable (Fig. 6a) and stable (Fig. 6b) conditions ($|U_x| \approx$ 8.7–9.0 m/s), which is somewhat expected because we employed the same initial conditions and mesoscale forcings for both. The difference lies in the wind shear, that is, the vertical change of U_x with height. The well-mixed unstable layer produces a flatter U_x profile, whereas the less mixed stable layer is associated with a large vertical gradient. This appears as the lighter blue color near the ground in Fig. 6b. An inspection of the color bar of the unstable case (Fig. 6a) reveals, on average, a positive value of 1 m/s near the ground. For stable conditions, this value is much smaller ($\approx$ 0.19 m/s), which suggests flow recirculation is enhanced during unstable conditions and is in agreement with the literature (Menke *et al.*, 2019).

The average potential temperature fields appear consistent with the simulation set-up and physical intuition. Temperatures near ground increase in the range between 300K and 305K for unstable conditions, rapidly decreasing with height

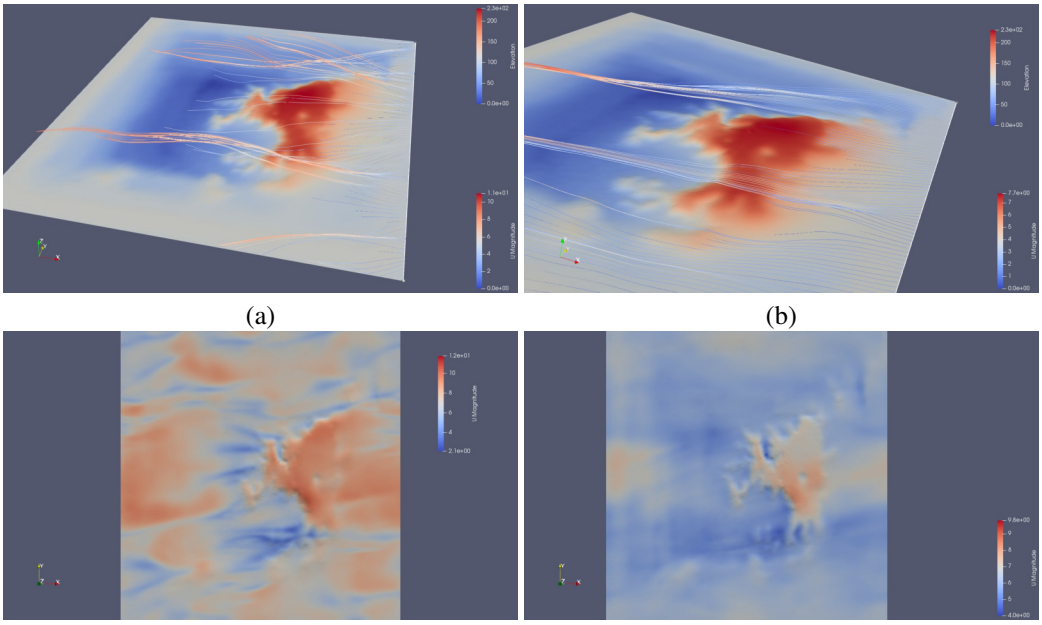

(a) (b)

(c) (d)

Figure 5. Streamlines passing through a horizontal line 10 m above ground level at the inlet for unstable (a) and stable (b) conditions reveal highly distinct wind patterns after 2 hours of simulation. The same patterns also appear in wind speed maps at 80 m above ground level as the formation of gusts in unstable conditions (c), whereas winds are gently-behaving in stable conditions (d).

toward the 300 K in the winds aloft (Fig. 6c). Conversely, temperatures near the ground cool down to a minimum of 296K and even more rapidly reach the 300K above ground. This is because vertical mixing in stable conditions is less effective than in unstable conditions. This fact is well illustrated in Figs. 6e-f as the enhancement in k (0–2.8 m^2 s^{-2}) for unstable conditions, in comparison with that of stable conditions (0–1.3 m^2 s^{-2}).

Figs. 7a-b show the mean power computed for the front and back rows based on 30-second wind speeds based on the CFD simulations for unstable conditions at the heights of 13 m and 82 m, respectively. The performance metric (ϵ_P) is computed as 10 min (twenty 30 s wind speeds) moving averages to mitigate the effects on unsteadiness on the interpretation of results. Even though the 13 m height is too low to be considered as hub height, we merely wish to compare to which extent the proximity to ground affects ϵ_P. The gusty nature of unstable winds presented in Figs. 5a and 5c appears here as violent fluctuations in the mean power at both rows. The latter gradually grow over time because of the positive synthetic mesoscale forcings.

At 13 m (Fig. 7a), ϵ_P oscillates between positive and negative values ultimately reaching an overall mean value of -10%. Closer to the actual turbine hub height (78 m) at 82 m (Fig. 7b) the mean power is considerably larger than in the former case because wind speeds increase with height. The fluctuations of ϵ_P are smoother and lead to a lower overall mean (ϵ_P = -3%). This lower $|\epsilon_P|$ at 82 m suggests that the influence of thermal circulations is higher near the ground, as these are ultimately responsible for the wind patterns that cause the performance differences. This is in accordance with the theoretical background (Hunt *et al.*, 2003) and observational evidence from wind tunnels (Monti *et al.*, 2002) and field experiments (Fernando *et al.*, 2019; Menke *et al.*, 2019; Mason, 2007).

Figs. 8a-b show the mean power computed for the front and back rows based on 30-second wind speeds based on the CFD simulations for stable conditions at the heights of 13 m and 82 m, respectively. The wind patterns during stable conditions produce performance patterns that largely differ from those shown in Figs 7a-b. Here, the mean power of the two rows steadily grows over time with little oscillations. This is a consequence of statically stable flows suppressing turbulent motion and producing the smooth streamlines reported herein (Figs. 5b).

In both Figs. 8a-b there are small-amplitude and high-frequency oscillations in the mean power of the back rows, which could arise owing to flow unsteadiness near the lee. At 13 m (Fig. 8a), ϵ_P is positive at all times and increases quickly to more than 50%. This produces an overall mean performance of 77%. At 82 m, ϵ_P grows with very little oscillation from about zero up to about 35% after 2 hours (Fig. 8b). Thus, the computed performance differences are larger near the ground than above, akin to the case of unstable conditions.

The initial conditions and mesoscale forcings are identical for the unstable and stable cases, the only difference lies in the heating or cooling of the ground surface. However, one can observe the significantly larger mean power during unstable conditions in comparison with stable conditions, at both heights. This is a probable consequence of the enhanced capability of unstable flows drawing in momentum from the top of the boundary layer, thus accelerating winds near the

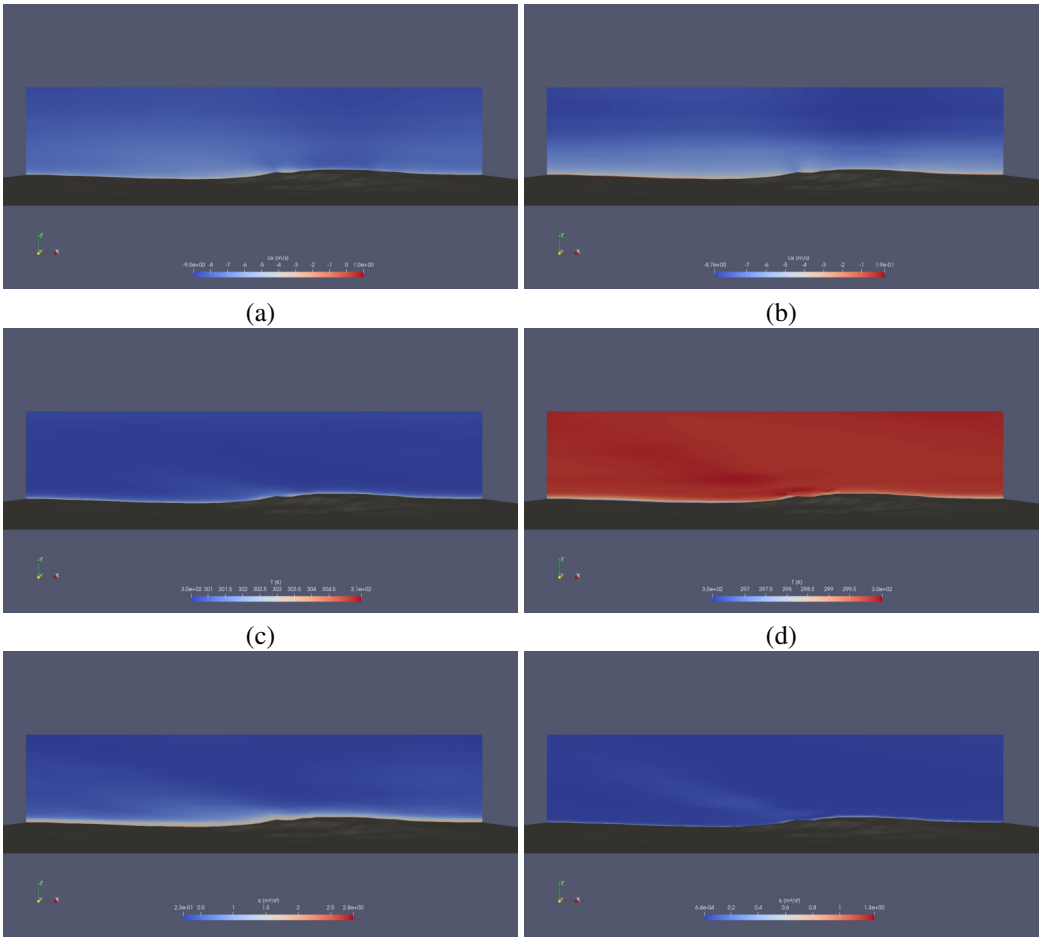

(a) (b) (c) (d) (e) (f)

Figure 6. Average U_x (a-b), T (c-d) and k (e-f) fields plotted on a vertical slice along the x-direction and centered at the domain origin were computed for the two-hour periods for the unstable and stable cases, respectively.

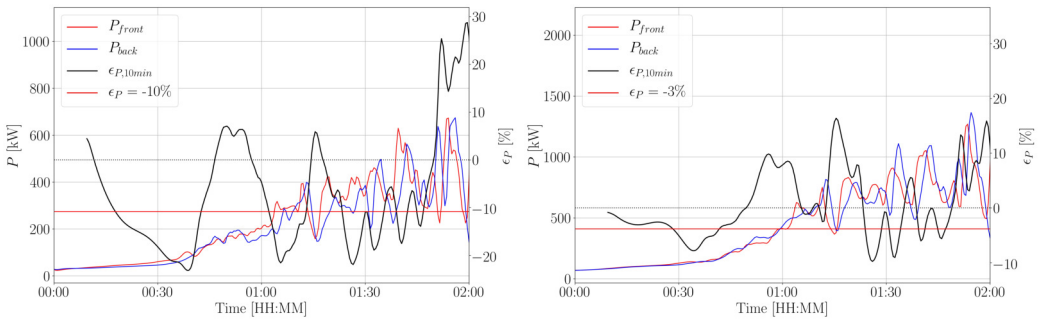

(a) (b)

Figure 7. Moving averages (10 min) of the power performance metric for unstable conditions at 13 m (a) and 82 m (b) above ground level computed based on 30 s wind speeds produce mean ϵ_P of -10% and -3%, respectively.

ground.

4. CONCLUSIONS

We assessed the employment of a novel simulation framework for wind energy application in complex terrain as a tool for evaluating the performance of an operational wind farm that was built over a small plateau area. Field measurements and wind farm production data gathered at the sited revealed a systematic overperformance of the back row during stable conditions. This pattern is inverted during unstable conditions and the same back rows underperform in comparison with the front rows. With this intent, two scenarios have been simulated with CFD. An unstably-stratified boundary-layer case that departs from an initially neutral condition (same potential temperature everywhere), the ground surface of

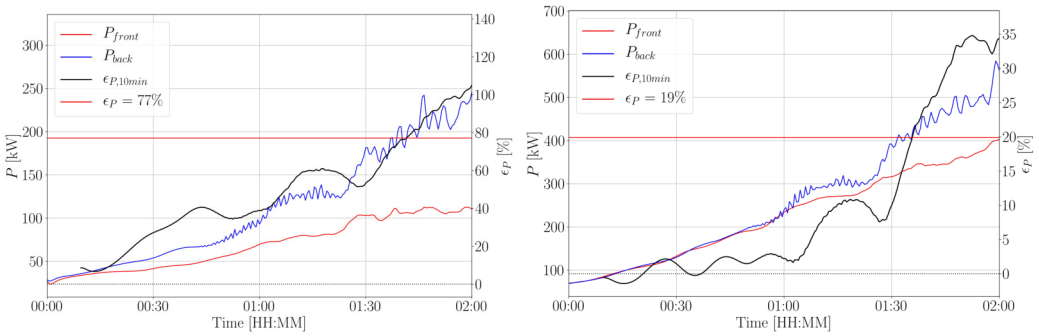

(a) (b)

Figure 8. Moving averages (10 min) of the power performance metric for stable conditions at 13 m (a) and 82 m (b) above ground level computed based on 30 s wind speeds produce mean ϵ_P of 77% and 19%, respectively.

which is heated up during a two-hour simulation run; and a stably-stratified boundary-layer case that also departs from neutral conditions, but where the ground surface is cooled down instead. Both simulations employed synthetic initial conditions and mesoscale forcings that are not intended to reproduce the wind conditions of the site accurately and in detail, but rather to perform a proof of concept: that the inversion in performance observed is explainable by the wind patterns and their interplay with atmospheric stability. Indeed, wind flow patterns are largely different between unstable and stable conditions and the numerical simulations are successful in emulating how the wind farm operates. Thus, these outcomes are encouraging in terms of the usage of mesoscale-to-microscale modeling frameworks that incorporate the effects of atmospheric stability for wind farm performance assessments and perhaps, in a near future, wind farm projects and resource assessment.

5. ACKNOWLEDGEMENTS

We would like to thank our R&D partner CGN Brasil Energia e Participações S.A., which provided valuable field observations and operational data for this research. The Brazilian National Council for Scientific and Technological Development (CNPq) is also highly regarded for financial support.

6. REFERENCES

Barthelmie, R.J. and Pryor, S.C., 2019. "Automated Wind Turbine Wake Characterization in Complex Terrain". *Atmospheric Measurement Techniques Discussions*, , No. January, pp. 1–31. doi:10.5194/amt-2018-461.

Chávez Arroyo, R., Irigoyen Indave, A., Sanz Rodrigo, J. and Fernandes Correia, P., 2018. "Analysis and validation of Weather Research and Forecasting model tendencies for meso-to-microscale modelling of the atmospheric boundary layer". *Journal of Physics: Conference Series*, Vol. 1037, No. 7. ISSN 17426596. doi:10.1088/1742-6596/1037/7/072012.

Fernando, H.J.S., Mann, J., Palma, J.M.L.M., Lundquist, J.K., Barthelmie, R.J., Belo-Pereira, M. and Brown et al., W.O.J., 2019. "The Perdigão: Peering into Microscale Details of Mountain Winds". *Bulletin of the American Meteorological Society*, Vol. 100, No. 5, pp. 799–819. ISSN 0003-0007. doi:10.1175/BAMS-D-17-0227.1.

Foken, T., 2006. "50 years of the Monin-Obukhov similarity theory". *Boundary-Layer Meteorology*, Vol. 119, No. 3, pp. 431–447. ISSN 00068314. doi:10.1007/s10546-006-9048-6.

Hunt, J.C.R., Fernando, H.J.S. and Princevac, M., 2003. "Unsteady Thermally Driven Flows on Gentle Slopes". *Journal of the Atmospheric Sciences*, Vol. 60, No. 17, pp. 2169–2182. ISSN 0022-4928. doi:10.1175/1520-0469(2003)060<2169:UTDFOG>2.0.CO;2.

Launder, B.E. and Spalding, D.B., 1974. "The numerical computation of turbulent flows". *Computer Methods in Applied Mechanics and Engineering*, Vol. 3, pp. 269–289. doi:10.1016/0045-7825(74)90029-2.

Lee, X., Massman, W. and Law, B., 2004. *Handbook of Micrometeorology: A guide for surface flux measurement and analysis*. Springer Science + Business Media, Inc. ISBN 1-4020-2265-4.

LI-COR Biosciences, 2019. "EddyPro Instruction Manual". URL `https://www.licor.com/documents/1ium2zmwm6hl36yz9bu4`.

Mann, J., Angelou, N., Arnqvist, J., Callies, D., Cantero, E., Chávez Arroyo, R., Courtney, M., Cuxart, J., Dellwik, E., Gottschall, J., Ivanell, S., Kühn, P., Lea, G., Matos, J.C., Palma, J.M., Pauscher, L., Peña, A., Sanz Rodrigo, J., Söderberg, S., Vasiljevic, N. and Veiga Rodrigues, C., 2017. "Complex terrain experiments in the New EuropeanWind Atlas". *Philosophical Transactions of the Royal Society A: Mathematical, Physical and Engineering Sciences*. ISSN 1364503X. doi:10.1098/rsta.2016.0101.

Mason, P.J., 2007. "Diurnal Variations In Flow Over A Succession of Ridges and Valleys". *Quarterly Journal of the Royal Meteorological Society*, Vol. 113, No. 478, pp. 1117–1140. ISSN 00359009. doi:10.1002/qj.49711347804.

Menke, R., Vasiljević, N., Mann, J. and Lundquist, J.K., 2019. "Characterization of flow recirculation zones at the Perdigão site using multi-lidar measurements". *Atmospheric Chemistry and Physics*, Vol. 19, No. 4, pp. 2713–2723. ISSN 1680-7324. doi:10.5194/acp-19-2713-2019. URL https://acp.copernicus.org/articles/19/2713/2019/.

Monin, A.S. and Obukhov, A.M., 1954. "Osnovnye zakonomernosti turbulentnogo pere- meshivanija v prizemnom sloe atmosfery (Basic Laws of Turbulent Mixing in the Atmo- sphere Near the Ground)". *Tr. Akad. Nauk SSSR Geofiz. Inst*, Vol. 24, No. 151, pp. 163–187.

Monti, P., Fernando, H.J.S., Princevac, M., Chan, W.C., Kowalewski, T.A. and Pardyjak, E.R., 2002. "Observations of Flow and Turbulence in the Nocturnal Boundary Layer over a Slope". *Journal of the Atmospheric Sciences*, Vol. 59, No. 17, pp. 2513–2534. ISSN 0022-4928. doi:10.1175/1520-0469(2002)059<2513:OOFATI>2.0.CO;2.

Radünz, W.C., Leite Mattuella, J.M. and Petry, A.P., 2020a. "Wind resource mapping and energy estimation in complex terrain: A framework based on field observations and computational fluid dynamics". *Renewable Energy*. ISSN 09601481. doi:10.1016/j.renene.2020.01.014. URL https://linkinghub.elsevier.com/retrieve/pii/S096014812030015X.

Radünz, W.C., Sakagami, Y., Haas, R., Petry, A.P., Passos, J.C., Miqueletti, M. and Dias, E., 2020b. "The variability of wind resources in complex terrain and its relationship with atmospheric stability". *Energy Conversion and Management*, Vol. 222, No. July, p. 113249. ISSN 01968904. doi:10.1016/j.enconman.2020.113249. URL https://doi.org/10.1016/j.enconman.2020.113249 https://linkinghub.elsevier.com/retrieve/pii/S0196890420307925.

Sanz Rodrigo, J., Allaerts, D., Avila, M., Barcons, J., Cavar, D., Chávez Arroyo, R.A., Churchfield, M., Kosovic, B., Lundquist, J.K., Meyers, J., Esparza, D.M., Palma, J., Tomaszewski, J.M., Troldborg, N., Van Der Laan, M.P. and Rodrigues, C.V., 2017a. "Results of the GABLS3 diurnal-cycle benchmark for wind energy applications". *Journal of Physics: Conference Series*, Vol. 854, No. 1. ISSN 17426596. doi:10.1088/1742-6596/854/1/012037.

Sanz Rodrigo, J., Chávez Arroyo, R.A., Moriarty, P., Churchfield, M., Kosović, B., Réthoré, P.E., Hansen, K.S., Hahmann, A., Mirocha, J.D. and Rife, D., 2017b. "Mesoscale to microscale wind farm flow modeling and evaluation". *Wiley Interdisciplinary Reviews: Energy and Environment*. ISSN 2041840X. doi:10.1002/wene.214.

Sanz Rodrigo, J., Churchfield, M. and Kosovic, B., 2017c. "A methodology for the design and testing of atmospheric boundary layer models for wind energy applications". *Wind Energy Science*, Vol. 2, No. 1, pp. 35–54. ISSN 2366-7451. doi:10.5194/wes-2-35-2017.

Silver, Z., Dimitrova, R., Zsedrovits, T., Baines, P.G. and Fernando, H.J.S., 2018. "Simulation of stably stratified flow in complex terrain: flow structures and dividing streamline". *Environmental Fluid Mechanics*, , No. 1573-1510. ISSN 1573-1510. doi:10.1007/s10652-018-9648-y. URL https://doi.org/10.1007/s10652-018-9648-y http://link.springer.com/10.1007/s10652-018-9648-y.

Sogachev, A., Kelly, M. and Leclerc, M.Y., 2012. "Consistent two-equation closure modelling for atmospheric research: Buoyancy and vegetation implementations". *Boundary-Layer Meteorology*, Vol. 145, No. 2, pp. 307–327. ISSN 15731472. doi:10.1007/s10546-012-9726-5.

Weller, H.G., Tabor, G., Jasak, H. and Fureby, C., 2002. "A tensorial approach to computational continuum mechanics using object-oriented techniques". *Computers in Physics*, Vol. 12, No. 6, p. 620. ISSN 08941866. doi:10.1063/1.168744.

Wharton, S. and Lundquist, J.K., 2012. "Assessing atmospheric stability and its impacts on rotor-disk wind characteristics at an onshore wind farm". *Wind Energy*, , No. 15, pp. 525–546. doi:10.1002/we.

7. RESPONSIBILITY NOTICE

The authors are solely responsible for the printed material included in this paper.